Available online at www.sciencedirect.com
SCIENCE DIRECT®
Journal of Computational Physics 207 (2005) 221–239
JOURNAL OF COMPUTATIONAL PHYSICS
www.elsevier.com/locate/jcp

Crystal growth of pure substances: Phase-field simulations in comparison with analytical and experimental results

B. Nestler [a], D. Danilov [a,*], P. Galenko [b]

[a] *Institute of Applied Research, Karlsruhe University of Applied Sciences, Moltkestrasse 30, 76133 Karlsruhe, Germany*
[b] *Institute of Space Simulation, German Aerospace Center, 51170 Cologne, Germany*

Received 20 July 2004; received in revised form 17 January 2005; accepted 18 January 2005
Available online 21 March 2005

Abstract

A phase-field model for non-isothermal solidification in multicomponent systems [SIAM J. Appl. Math. 64 (3) (2004) 775–799] consistent with the formalism of classic irreversible thermodynamics is used for numerical simulations of crystal growth in a pure material. The relation of this approach to the phase-field model by Bragard et al. [Interface Science 10 (2–3) (2002) 121–136] is discussed. 2D and 3D simulations of dendritic structures are compared with the analytical predictions of the Brener theory [Journal of Crystal Growth 99 (1990) 165–170] and with recent experimental measurements of solidification in pure nickel [Proceedings of the TMS Annual Meeting, March 14–18, 2004, pp. 277–288; European Physical Journal B, submitted for publication]. 3D morphology transitions are obtained for variations in surface energy and kinetic anisotropies at different undercoolings. In computations, we investigate the convergence behaviour of a standard phase-field model and of its thin interface extension at different undercoolings and at different ratios between the diffuse interface thickness and the atomistic capillary length. The influence of the grid anisotropy is accurately analyzed for a finite difference method and for an adaptive finite element method in comparison.

PACS: 81.30.Fb; 68.70.+w; 81.10.Aj; 02.70.−c

Keywords: Phase-field modelling; Growth morphologies; Numerical simulation; Crystal growth

1. Introduction

Crystal growth phenomena and the shapes of growing crystals are of fundamental interest to physicists and are of practical importance to engineers [6]. Within the field of investigating solidification processes, a

* Corresponding author. Fax: +49 721 925 2361.
E-mail addresses: britta.nestler@fh-karlsruhe.de (B. Nestler), denis.danilov@fh-karlsruhe.de (D. Danilov), peter.galenko@dlr.de (P. Galenko).

0021-9991/$ - see front matter © 2005 Elsevier Inc. All rights reserved.
doi:10.1016/j.jcp.2005.01.018

great progress has been made in the past. However, several fundamental problems still remain unsolved. One of the open questions is a quantitative modelling of crystal growth in a wide spectrum of undercoolings and of solidification velocities (see [7] and references therein).

In order to model and numerically simulate crystal growth processes in 3D under various solidification conditions, we apply a diffuse interface formulation for solidification that is based on the phase-field methodology. The first phase-field models were suggested about twenty years ago in [8–11]. The formulation was further developed to describe phase transitions in condensed media with diffuse phase boundaries by Penrose and Fife [12]. Nowadays, the phase-field method has emerged as a powerful tool that enables the modelling of complex pattern formations for the first time. The concept has been validated by comparison with theoretical predictions and experimental measurements and is applied to a broad range of investigations in materials science [13].

In contrast to sharp interface approaches with interfaces of zero thickness, the phase-field model introduces a new smooth variable $\phi(\vec{x},t)$ replacing the sharp interface by a diffuse interface profile. In the diffuse interface formulation, the phase field $\phi(\vec{x},t)$ has a constant value within the bulk phases, e.g., $\phi(\vec{x},t)=0$ in the liquid and $\phi(\vec{x},t)=1$ in the solid phase. In regions of phase boundaries, the phase field $\phi(\vec{x},t)$ changes steeply but smoothly from 0 to 1. The position of the interface is located at $\phi(\vec{x},t)=1/2$. The diffuse profile enables to avoid the explicit tracking of the interface. Consequently, the phase field ϕ is considered as an order parameter which is introduced to describe the moving interfacial boundary between unstable and stable phases during phase transformation processes. By asymptotic expansions, it can be shown that the phase-field methods relate to classical sharp interface models such as Hele–Shaw type models and Stefan problems in the limit of zero interfacial thickness, e.g. [14]. Beginning from the work of Kobayashi [15], phase-field models have been applied to dendritic patterns in pure metals and in binary alloy solidification at small and moderate undercoolings (see details in the overview [16]). However, a quantitative comparison of simulated crystal patterns with experimental findings and theoretical predictions has only recently been started. Further evaluation of the modelling results obtained using the phase-field method in comparison with experimental data and, especially, with analytical solutions from the theory of crystal growth is one of the actual problems of computational physics in materials science.

In this paper, we apply the phase-field model formulated for multiphase and multicomponent solidification [1] to crystal growth in a pure substance and relate this model to the thin interface approximation by Bragard et al. [2]. The convergence behaviour of the "standard" phase-field model in comparison with the "thin interface" solution is analyzed for planar front growth. A finite difference and a finite element discretization for solving the evolution equations is proposed and the influence of the numerical grid on the structure formation is examined for both methods. The general accuracy of the numerical methods that can be expected for investigating dendritic crystal growth from undercooled melt will be discussed. Quantitatively, the dendrite tip velocities and the dendrite tip radii are evaluated within a wide range of undercoolings and growth velocities. Subsequently, the phase-field simulations of dendritic solidification in 2D and 3D are compared with analytical results by Brener [3] and with recent experimental observations summarized in [4,5]. Finally, a variety of 3D morphologies predicted by phase-field simulations is presented showing grained, dendritic, fractal and globular (spherical) shapes.

2. Phase-field modelling

2.1. General model equations

For our numerical simulations, we use the phase-field model that has recently been proposed by Garcke, Nestler and Stinner [1]. This model is consistent with classical irreversible thermodynamics and describes

phase transformations in non-isothermal multicomponent and multiphase systems. The formulation is based on an entropy density functional

$$\mathscr{S}(e,\boldsymbol{c},\boldsymbol{\phi}) = \int_{\Omega}\left(s(e,\boldsymbol{c},\boldsymbol{\phi}) - \left(\varepsilon a(\boldsymbol{\phi},\nabla\boldsymbol{\phi}) + \frac{1}{\varepsilon}w(\boldsymbol{\phi})\right)\right)\mathrm{d}x. \tag{1}$$

For general alloy systems with K components and N phases, the bulk entropy density s depends on the concentrations of the components $\boldsymbol{c}(\vec{x},t) = (c_k(\vec{x},t))_{k=1,\ldots,K}$, on the phase-field variables $\boldsymbol{\phi}(\vec{x},t) = (\phi_\alpha(\vec{x},t))_{\alpha=1,\ldots,N}$ and on the inner energy density e. The variable $\phi_\alpha(\vec{x},t)$ denotes the local fraction of phase α. The contributions $a(\boldsymbol{\phi},\nabla\boldsymbol{\phi})$ and $w(\boldsymbol{\phi})$ of the entropy functional reflect the thermodynamics of the interfaces and ε is a small length scale parameter related to the thickness of the diffuse interface.

For modelling dendritic growth from an undercooled pure substance, the system of variables reduces to one component $c = 1$ and to two phase fields ϕ_1 (solid) and ϕ_2 (liquid). Since the variables fulfill the constraint $\phi_1 + \phi_2 = 1$, a single phase-field variable $\phi = \phi_1$ is sufficient to describe the evolution of the phase boundaries in the system. The set of governing equations for the energy conservation and for the non-conserved phase-field variable ϕ can be derived from Eq. (1) by taking the functional derivatives $\delta\mathscr{S}/\delta e$ and $\delta\mathscr{S}/\delta\phi$ in the following form

$$\frac{\partial e}{\partial t} = -\nabla\cdot\left\{L_{00}(T,\phi)\nabla\frac{\delta\mathscr{S}}{\delta e}\right\}, \quad \text{energy conservation,} \tag{2}$$

$$\omega\varepsilon\frac{\partial\phi}{\partial t} = \frac{\delta\mathscr{S}}{\delta\phi}, \quad \text{phase-field equation,} \tag{3}$$

where ω is a kinetic mobility. In the case of anisotropic kinetics, ω is a function of $\nabla\phi$ and, hence, depends on the orientation of the phase boundary. $\nabla\cdot\{L_{00}(T,\phi)\nabla(\delta\mathscr{S}/\delta e)\}$ denotes a divergence operator. The mobility coefficient $L_{00}(T,\phi)$ is related to the heat conductivity $\kappa(\phi)$. For simplicity, we assume κ to be constant $\kappa(\phi) = \kappa$ and write $L_{00} = \kappa T^2$. We make the ansatz $e = -\Delta H p(\phi) + c_v T$ with a latent heat ΔH and a constant specific heat c_v. Since $\delta\mathscr{S}/\delta e = T^{-1}$ for pure substances, we obtain from Eq. (2) the governing equation for the temperature T. This yields

$$\frac{\partial T}{\partial t} = a\nabla^2 T + T_{\mathrm{Q}}\frac{\partial p(\phi)}{\partial t}, \tag{4}$$

where $a = \kappa/c_v$ is the thermal diffusivity and $T_{\mathrm{Q}} = \Delta H/c_v$ is the adiabatic temperature. From Eq. (3), the phase-field equation follows by using the thermodynamic relation $e = f + Ts$

$$\omega\varepsilon\frac{\partial\phi}{\partial t} = \varepsilon\nabla\cdot a_{,\nabla\phi}(\nabla\phi) - \frac{1}{\varepsilon}w_{,\phi}(\phi) - \frac{f_{,\phi}(T,\phi)}{T}, \tag{5}$$

where $a_{,\nabla\phi}$, $w_{,\phi}$ and $f_{,\phi}$ denotes the partial derivative with respect to $\nabla\phi$ and ϕ, respectively. The free energy densities are expressed as

$$w(\phi) = \gamma m g(\phi), \quad \text{double well potential,} \tag{6}$$

$$f(T,\phi) = \Delta H\frac{T - T_{\mathrm{M}}}{T_{\mathrm{M}}}p(\phi), \quad \text{bulk free energy density,} \tag{7}$$

$$a(\nabla\phi) = \frac{\gamma}{m}a_{\mathrm{c}}^2(\nabla\phi)|\nabla\phi|^2, \quad \text{gradient energy density,} \tag{8}$$

where T_{M} is the melting temperature, γ defines the surface entropy value of the solid–liquid interface and m is a mobility parameter. The polynomial functions $g(\phi)$ and $p(\phi)$ are given by

$$g(\phi) = -\tfrac{1}{2}(2\phi-1)^2 + \tfrac{1}{4}(2\phi-1)^4, \tag{9}$$

$$p(\phi) = (2\phi - 1) - \tfrac{2}{3}(2\phi - 1)^3 + \tfrac{1}{5}(2\phi - 1)^5. \tag{10}$$

The anisotropy of the surface energy is realized by the factor $a_c(\nabla\phi)$ and we assume consistency with an underlying cubic symmetry of the material

$$a_c(\nabla\phi) = 1 - 3\epsilon_c + 4\epsilon_c \frac{1}{|\nabla\phi|^4} \sum_i \left(\frac{\partial\phi}{\partial x_i}\right)^4, \tag{11}$$

where ϵ_c is the magnitude of the capillary anisotropy and $\partial/\partial x_i$ is the partial derivative with respect to the Cartesian coordinate axis x_i, $i = 1, 2, 3$. Taking the derivatives $a_{,\nabla\phi}$, $w_{,\phi}$ and $f_{,\phi}$ of the energy densities in Eqs. (6) and (8), the phase-field Eq. (5) reads

$$2\omega\varepsilon^2 \frac{\partial\phi}{\partial t} = \frac{2\gamma\varepsilon^2}{m}\left(\nabla(a_c^2\nabla\phi) + \sum_i \frac{\partial}{\partial x_i}\left(|\nabla\phi|^2 a_c \frac{\partial a_c}{\partial(\partial_{x_i}\phi)}\right)\right) - \gamma m \frac{\mathrm{d}g(\phi)}{\mathrm{d}\phi} - \varepsilon\Delta H \frac{T - T_M}{TT_M}\frac{\mathrm{d}p(\phi)}{\mathrm{d}\phi}. \tag{12}$$

The anisotropy of the interface kinetics can be introduced by ω depending on the vector $\nabla\phi$ in an analogous way as in Eq. (11) for the surface energy.

2.2. Relation to the thin interface model

In this section, we derive the relation between the phase-field model given by Eqs. (4) and (12) and the model proposed by Bragard et al. [2]. First, we introduce a dimensionless temperature u and a new phase-field variable ψ rescaled with a transition $-1 \leqslant \psi \leqslant 1$ by

$$u = \frac{T - T_M}{T_Q} \quad \text{and} \quad \psi = 2\phi - 1.$$

With these definitions, the polynomial functions $g(\psi)$ and $p(\psi)$ in Eqs. (9) and (10) rewrite to

$$g(\psi) = -\frac{\psi^2}{2} + \frac{\psi^4}{4}, \quad \text{and} \quad p(\psi) = \psi - \frac{2\psi^3}{3} + \frac{\psi^5}{5}.$$

By comparing the energy densities and the governing equations, we find the following parameter relations between the two models:

(i) Surface entropy density γ, mobility m and diffuse interface thickness ε:

$$\gamma = \frac{\sqrt{2}}{a_1}\frac{\sigma_0}{T_M}, \quad m = \frac{1}{\gamma}, \quad \text{and} \quad \varepsilon = \frac{a_1 T_M}{\sigma_0} W_0, \tag{13}$$

where σ_0 is the surface tension and $a_1 = 5\sqrt{2}/8$ is a constant parameter computed in [17].

(ii) Kinetic coefficient $\tau(\nabla\psi)$ and time scaling factor τ_0:

$$\frac{\omega\varepsilon^2}{2} = \tau(\nabla\psi) = \tau_0 a_c(\nabla\psi) a_k(\nabla\psi)\left(1 + a_2 \frac{\lambda d_0}{a\beta_0}\frac{a_c(\nabla\psi)}{a_k(\nabla\psi)}\right), \tag{14}$$

$$\text{with} \quad \tau_0 = \frac{\beta_0 \lambda^2 d_0}{a_1^2}, \tag{15}$$

where $\beta_0 = 1/(\mu T_Q)$ with a kinetic coefficient μ and $a_2 = 0.6267$ is a dimensionless model constant depending only on the choice of the functions $g(\phi)$ and $p(\phi)$ in Eqs. (5)–(8) and, for our case, it has been computed in [17]. Similarly as in Eq. (11), the factor a_k can depend on $\nabla\psi$ in order to model kinetic anisotropy, such that

$$a_k(\nabla\psi) = 1 + 3\epsilon_k - 4\epsilon_k \frac{1}{|\nabla\psi|^4} \sum_i \left(\frac{\partial\psi}{\partial x_i}\right)^4.$$

(iii) Microscopic capillary length d_0 and coupling parameter λ in the free energy functions:

$$d_0 = \frac{\sigma_0 T_M c_v}{\Delta H^2} = a_1 \frac{W_0}{\lambda}, \quad \text{and} \quad \lambda = \frac{\varepsilon \Delta H T_Q}{T_M^2} = \frac{\varepsilon \Delta H^2}{c_v T_M^2}. \tag{16}$$

Using Eqs. (13)–(16) and the approximations

$$\frac{T_Q u}{T_M} \ll 1 \quad \text{and} \quad \frac{u}{1 + \frac{T_Q u}{T_M}} \simeq u,$$

we obtain the governing equations

$$\frac{\partial u}{\partial t} = a\nabla^2 u + \frac{1}{2}\frac{\partial p(\psi)}{\partial t}, \tag{17}$$

$$\tau \frac{\partial\psi}{\partial t} = W_0^2 \nabla(a_c^2 \nabla\psi) + W_0^2 \sum_i \frac{\partial}{\partial x_i}\left(|\nabla\psi|^2 a_c \frac{\partial a_c}{\partial(\partial_{x_i}\psi)}\right) - \frac{\partial g(\psi)}{\partial\psi} - \lambda u \frac{\partial p(\psi)}{\partial\psi}. \tag{18}$$

Here, we have used the "thin interface" ($a_2 \neq 0$) analysis of the phase-field model developed by Karma and Rappel [17] in which the interface thickness W_0 is assumed to be small compared to the scale of the crystal pattern, but larger than the microscopic capillary length d_0. The thin interface limit is suited for quantitative modelling of dendritic growth in pure materials at low undercoolings in conjunction with efficient numerical algorithms [18]. Bragard et al. [2] presented phase-field simulations by means of the version of the thin interface analysis [17] extended for numerical investigations of pattern formations for both small and high undercoolings in pure systems. In their article, the authors point out the necessity of introducing a nonlinear function $h(\lambda u)$ to the phase-field equation to recover the linear relationship between the growth rate and the interface undercooling. The nonlinear function $h(\lambda u)$ can be considered as a renormalization of the driving force of the free energy. This renormalization depends on the choice of the interface thickness in a nonlinear way. Therefore, the bulk free energy densities are changed with varying interface thickness. The introduction of the renormalization function $h(\lambda u)$ cannot be derived from a fundamental thermodynamical potential, but it enables the use of interface thicknesses suitable for phase-field simulations. The corresponding evolution equation for the phase field reads

$$\tau \frac{\partial\psi}{\partial t} = W_0^2 \nabla(a_c^2 \nabla\psi) + W_0^2 \sum_i \frac{\partial}{\partial x_i}\left(|\nabla\psi|^2 a_c \frac{\partial a_c}{\partial(\partial_{x_i}\psi)}\right) - \frac{\partial g(\psi)}{\partial\psi} - h(\lambda u)\frac{\partial p(\psi)}{\partial\psi}. \tag{19}$$

2.3. Material and model parameters

The system of governing equations for the evolution of the temperature and of the phase field (Eqs. (4) and (12)) can be used to quantitatively model dendritic growth and morphological transformations. Experimentally measured material constants are inserted into the phase-field model. Thermophysical properties for pure nickel have been obtained by Barth et al. [19] using calorimetric methods in the metastable regime of an undercooled melt. The results have been tested by Eckler and Schwarz [20,21] in a number of verifications of the sharp interface models in comparison with the experimental data. The values of surface

Table 1
Two sets of thermophysical material data used for the phase-field simulations of dendritic growth from a pure nickel melt

Parameter	Symbol [dimension]	Data set 1 [reference]	Data set 2 [reference]
Melting temperature	T_M [K]	1728, [29]	1726, [2]
Latent heat	ΔH [J/m^3]	8.113×10^9, [19]	2.311×10^9, [2]
Specific heat	c_v [J/(m^{3}K)]	1.939×10^7, [19]	5.313×10^6, [2]
Thermal diffusivity	a [m^2/s]	1.2×10^{-5}, [20,21]	10^{-5}, [2]
Interfacial free energy	σ_0 [J/m^2]	0.326, [23]	0.326, [2]
Strength of interfacial energy	ϵ_c [–]	0.018, [2,23]	0.018, [2]
Growth kinetics in ⟨1 0 0⟩-crystallographic direction	μ_{100} [m/(sK)]	0.52, [22]	0.52, [2]
Growth kinetics in ⟨1 1 0⟩-crystallographic direction	μ_{110} [m/(sK)]	0.40, [22]	0.40, [2]

Table 2
Two computed sets of parameters for phase-field modelling of dendritic growth of nickel crystals derived from the two data sets in Table 1

Parameter	Symbol [dimension]	Relation	Data set 1	Data set 2
Adiabatic temperature	T_Q [K]	$\Delta H/c_v$	418	435
Capillary length	d_0 [m]	$\sigma_0 T_M/(\Delta H T_Q)$	1.659×10^{-10}	5.56×10^{-10}
Averaged kinetic coefficient	β_0 [s/m]	$(\mu_{100}^{-1} + \mu_{110}^{-1})/(2T_Q)$	5.3×10^{-3}	5.084×10^{-3}
Strength of the kinetic anisotropy	ϵ_k [–]	$(\mu_{100} - \mu_{110})/(\mu_{100} + \mu_{110})$	0.13	0.13

energy, atomic attachment kinetics and their anisotropies are taken from data of atomistic simulations by Hoyt et al. [22,23] which have been linked with the phase-field simulations for analysis of dendritic growth in a wide range of undercoolings [2,24]. It is remarkable to note that the values for the atomic kinetics given by atomistic simulations [22,24] are approximately four to five times lower than those predicted by the collision-limited theory of interface advancing [25] which can be rather well compared with the values found from previous molecular dynamic simulation data of Broughton et al. [26]. Also, to adjust the kinetics of rapid dendritic growth of nickel based alloys, Galenko and Danilov [27,28] stated that the fit to experimental data is obtained only if the crystal growth kinetics is found to be a factor of five less than it is predicted by the theory of collision-limited growth [25]. These outcomes might be explained due to a more complicated behaviour of the atomic ensemble fluctuations around the interface leading to slower kinetics in comparison with the ideal situation considered by the collision-limited theory. Two sets of material parameters according to different references are used for our simulations of pure nickel solidification in comparison. The values are given in Table 1.

From these data, we computed two sets of parameters for the phase-field model in Eqs. (4) and (12) such as the microscopic capillary length d_0, the adiabatic temperature T_Q, the averaged kinetic coefficient β_0, and the strength ϵ_k of the kinetic anisotropy. The values of these parameters are specified in Table 2 and used for both, the phase-field model and the analytical solutions for the crystal growth. The tilt of the free energy well is increased within the range $\lambda = 1$–18, while decreasing the dimensionless undercooling $\Delta = (T - T_M)/T_Q = 1.30$–0.10. For these values of λ, we determined the time scale for the phase-field kinetics from the expression $\tau_0 = \lambda^2 d_0 \beta_0 / a_1^2$ and the parameter of the interface thickness from the expression $W_0 = \lambda d_0 / a_1$.

3. Numerical solving methods

The set of evolution equations are solved numerically by applying two different numerical methods: A finite difference method (FDM) and a finite element method (FEM) with an adaptive grid generator.

Results obtained with both methods are presented and the influence of the grid anisotropy is investigated in Section 5. For the computations, we introduce dimensionless variables $x = x'/L_s$ and $t = t/\tau_s$ with a space scale L_s and a time scale τ_s. Further, for simplicity we assume a linear function $p(\psi) = \psi$ in the equation for the temperature field as in [17] and rewrite Eqs. (17) and (19) in dimensionless form

$$\frac{\partial u}{\partial t} = \frac{\tau_s}{L_s^2} a \nabla^2 u + \frac{1}{2}\frac{\partial \psi}{\partial t}, \tag{20}$$

$$\frac{\tau}{\tau_s}\frac{\partial \psi}{\partial t} = \frac{W_0^2}{L_s^2}\nabla(a_c^2 \nabla\psi) + \frac{W_0^2}{L_s^2}\sum_i \frac{\partial}{\partial x_i}\left(|\nabla\psi|^2 a_c \frac{\partial a_c}{\partial(\partial_{x_i}\psi)}\right) - \frac{\partial g(\psi)}{\partial \psi} - h(\lambda u)\frac{\partial p(\psi)}{\partial \psi}. \tag{21}$$

Homogeneous Neumann conditions for u and ψ are used at the boundaries of the rectangular computational domains. To compute the function $h(\lambda u)$ we used a table of numerical data obtained from the iteration method described in [2,30].

3.1. Finite difference method

A finite difference algorithm with an explicit time marching scheme as previously described in [31] has been implemented to solve the heat equation and the phase-field equation on a uniform numerical grid. The 3D dendritic growth structures shown in Section 6.2 are simulated on the basis of this discretization method. We assume equal grid spacings of the three dimensions, i.e. $\Delta x = \Delta y = \Delta z$ and we introduce the notation i, j, k for the spatial coordinates of the Cartesian origin and n for indicating the number of numerical time steps. Typical values for the grid spacing Δx and for the time step Δt are $\Delta x = 0.85\ W_0$ and $\Delta t = 4.52 \times 10^{-4}\tau_0$. For space and time scaling parameters, we choose $\tau_s = \tau_0$ and $L_s = W_0$.

3.2. Finite element method

As outlined by Provatas et al. [32], a numerical method based on an adaptive mesh refinement discretization exhibits a computationally efficient technique to solve the phase-field equations describing the evolution and dynamics of phase boundaries. To employ a finite element discretization, the evolution equations for u and ψ are solved in a weak form with a semi-implicit time scheme. Using the same time and space scaling as in the case of finite differences and applying homogeneous Neumann conditions at the domain boundaries, the integral of Eqs. (20) and (21) over a domain Ω gives

$$\int_\Omega \left(u^{n+1} - \frac{1}{2}\psi^{n+1}\right)\xi \,\mathrm{d}\Omega + \frac{a\tau_0 \Delta t}{W_0^2}\int_\Omega \nabla u^{n+1}\nabla\xi \,\mathrm{d}\Omega = \int_\Omega \left(u^n - \frac{1}{2}\psi^n\right)\xi \,\mathrm{d}\Omega \tag{22}$$

and

$$\begin{aligned}&\int_\Omega \frac{\tau(\nabla\psi^n)}{\tau_0}\psi^{n+1}\xi \,\mathrm{d}\Omega + \Delta t\int_\Omega a_c^2(\nabla\psi^n)\nabla\psi^{n+1}\nabla\xi \,\mathrm{d}\Omega \\ &\quad = \int_\Omega \frac{\tau(\nabla\psi^n)}{\tau_0}\psi^n\xi \,\mathrm{d}\Omega - \Delta t\left(\int_\Omega \vec{\mathcal{N}}^n\nabla\xi \,\mathrm{d}\Omega - \int_\Omega\left[\left(\frac{\partial g(\psi)}{\partial\psi}\right)^n - h(\lambda u^n)\left(\frac{\partial p(\psi)}{\partial\psi}\right)^n\right]\xi \,\mathrm{d}\Omega\right),\end{aligned} \tag{23}$$

where ξ is a test function and $\vec{\mathcal{N}}$ is defined by

$$\vec{\mathcal{N}}^n_{i,j,k} = \left(|\nabla\psi|^2 a_c\left(\frac{\partial a_c}{\partial(\partial_x\psi)}, \frac{\partial a_c}{\partial(\partial_y\psi)}, \frac{\partial a_c}{\partial(\partial_z\psi)}\right)\right)^n_{i,j,k}. \tag{24}$$

In this form, Eqs. (22) and (23) are discretized as a system of linear equations with respect to the implicit terms $\sim\psi^{n+1}$ and $\sim u^{n+1}$.

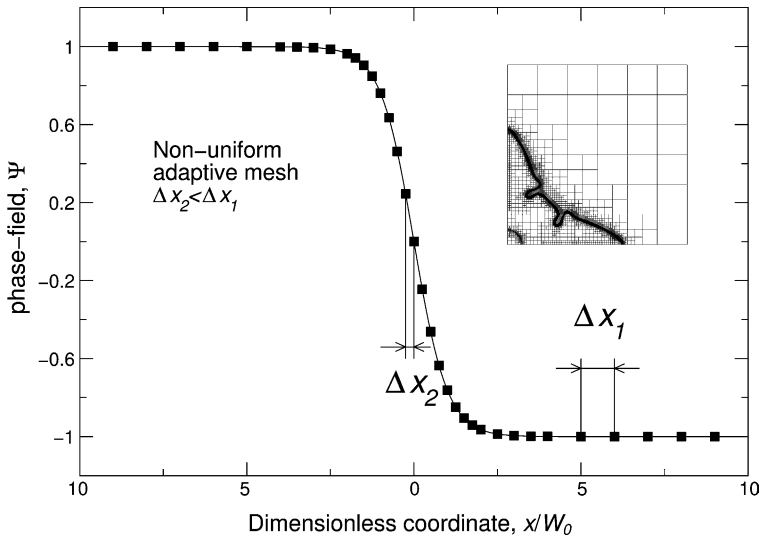

Fig. 1. Non-uniform adaptive grid with a finer spacing Δx_2 at the diffuse solid–liquid interface and a larger spacing Δx_1 away from the interface. The inlay shows the applied mesh for resolving dendritic growth.

To resolve the interfaces in the phase-field model, the grid spacing Δx must be smaller than the characteristic interface thickness W_0. On the other hand, the computational domain size L is determined by the characteristic scale of the diffusion fields with a typical ratio of $L/W_0 \sim 10^2$–10^4. To achieve high spatial resolution only in regions of a smooth but strongly localized transition of the phase field ψ from -1 to 1, a local gradient indicator E is used to selectively refine or coarsen the mesh

$$E = (|\nabla\psi| + E_T|\nabla T|)d^2, \tag{25}$$

where d is the diagonal of a numerical cell. The adaptive grid generator supplied by deal II [33] refines a cell if $E > E_{max} = 2 \times 10^{-5}$, and it coarsens a cell if $E < E_{min} = 5 \times 10^{-6}$, with $E_T = 0.1$. By this choice we obtain $d \sim 1/\sqrt{E}$. Fig. 1 illustrates the non-uniform adaptive grid with a different degree of grid fineness along the profile of the phase-field variable. The embedded inlay gives an impression of the numerical mesh used for computing dendrites. In the region of the diffuse interface thickness, a higher resolution is realized by a smaller grid spacing $\Delta x_2 < \Delta x_1$.

4. Comparison of thin and sharp interface asymptotics

The application of a phase-field model for computing solidification phenomena of the order of micrometers is always accompanied by a discussion about the two different length scales involved in such a process. On the one hand, the diffuse interface description of a phase-field model contains interfaces of a diffuse thickness W_0 on a micrometer scale. On the other hand, a solid–liquid interface has a real atomistic capillary length d_0 of the order of nanometers. Due to computing time and memory resources, simulations of, e.g., dendritic or eutectic structures are only feasible for diffuse interface thicknesses much larger than the atomistic scale. Within the context of this scaling problem, we investigate the ability of the two types of asymptotics for phase-field models: The sharp interface limit as a first order asymptotic and the thin interface approach as a second order asymptotic. We performed computations of a planar solid–liquid interface

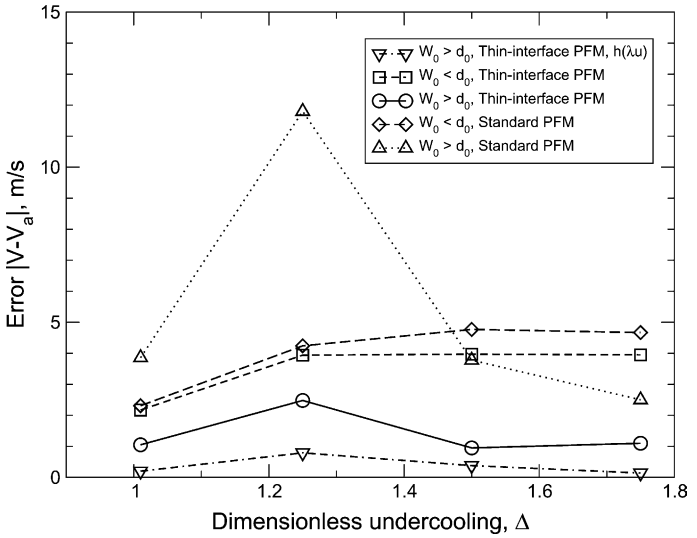

Fig. 2. The simulated velocity v with respect to the analytical prediction v_a on the dimensionless undercooling. The simulation results of a growing planar solid–liquid interface in pure nickel correspond to the diffuse interface thickness W_0 smaller and larger than the microscopic capillary length d_0 using a standard phase-field model ($a_2 = 0$ in Eq. (14)) (symbols: Δ, $\diamond$), a thin interface extension ($a_2 \neq 0$ in Eq. (14)) (symbols: $\bigcirc$, $\square$) and a thin interface formulation plus the renormalization function $h(\lambda u)$ (symbol: ∇).

of pure nickel for the two cases $W_0 > d_0$ and $W_0 < d_0$. The simulated results are compared with the exact analytical expression for the growth velocity v_a of a planar interface given by

$$\beta_0 v_a = \Delta - 1,$$

where $\Delta = (T_M - T_0)/T_Q$ is the dimensionless initial undercooling, T_0 is the temperature far from the interface according to $T_0 = T_I - T_Q$ with T_I being the temperature of the interface. To determine the analytical values for the velocity, we use β_0, T_M and T_Q listed in Tables 1 and 2 (data set 1). Fig. 2 shows the results of a series of simulations for $W_0 = 0.43d_0 < d_0$ and $W_0 = 2.34d_0 > d_0$ using a standard and a thin interface phase-field model in comparison. For the case $W_0 > d_0$, the thin interface solution gives a better convergence than the standard phase-field model, whereas for $W_0 < d_0$, the values of the velocities are almost the same for both asymptotics. Moreover, as expected for the case $W_0 > d_0$, it can be seen in (Fig. 2) that the disagreement between the predictions of the numerical simulations and the sharp-interface analytical solution reduces significantly by considering the sequence "$W_0 > d_0$, standard PFM (symbol: $\triangle$)" → "$W_0 > d_0$, thin-interface PFM (symbol: $\bigcirc$)" → "$W_0 > d_0$, thin-interface PFM (symbol: $\bigtriangledown$) with renormalization function $h(\lambda u)$" as in Eq. (21).

5. Investigation of grid anisotropy

To analyze the influence of grid anisotropy on the shape of the structure, we have performed numerical simulations of a stationary spherical and isotropic particle ($\epsilon_c = 0$, $\epsilon_k = 0$) comparing both numerical methods: FDM and FEM. We have adjusted the parameters of the simulations according to the Gibbs–Thomson condition so that the initial radius of a sphere is stable in size. This is equivalent to the condition that curvature undercooling equals kinetic undercooling. The stability of the spherical particle is guarantied (also numerically) by solving the coupled system of the temperature and phase-field equations. A small

movement of the particle interface leads to a release or adsorption of latent heat which suppresses further development of instability. Different radii were chosen initially and the final $\psi = 0$ isoline was interpolated. We measured the final radius in alignment with the numerical grid denoted by R_{100} and at a 45° angle to the grid denoted by R_{110}, see Fig. 3.

From the two radii R_{100} and R_{110}, we obtain an estimation for the grid anisotropy

$$\varepsilon_g = \frac{R_{110} - R_{100}}{R_{110} + R_{100}}.$$

For the FDM and FEM simulation setup, we chose a computational domain size of 10^{-6} m, a thickness of the solid–liquid interface $W_0 = 1.127 \times 10^{-9}$ m and a grid scale $\Delta x = 9.67 \times 10^{-10}$ m. In the case of an adaptive finite element grid, the value Δx corresponds to the smallest grid cell. We investigated the effect of grid anisotropy for five different initial radii R_0. The results are illustrated in Fig. 4. It can be seen that the influence of grid anisotropy ε_g is smaller for larger initial crystals. In the considered range of radii, the grid anisotropy ε_g approaches a constant value of 0.01% for increasing radii. For smaller radii, the influence of the numerical grid and equivalently the deviation from an isotropic spherical solid–liquid interface is more pronounced. In the computations, the grid anisotropy ε_g lies in the interval 0.01–0.1% for radii $R_0/\Delta x$ from 100 to 550. For smaller dimensionless radii $R_0/\Delta x$ from 15 to 60, Karma and Rappel [17] stated a grid anisotropy of approximately 5.0%. Since the physical anisotropies for the surface energy and for the kinetics are $\epsilon_c = 1.8\%$ and $\epsilon_k = 13\%$, we conclude that the grid anisotropy may effect the growth of a crystal at the beginning stages of solidification for small undercoolings. In other words, the grid anisotropy has a non-negligible influence on the shape of a crystal for small crystal seeds or for crystal growth at relatively small undercoolings. In the latter case, the direction of growth is dictated by the anisotropy of the surface energy. For all other cases of crystal growth, with dimensionless radii of a crystal greater than 100 grid spacings and with an evolution proceeding under the influence of both physical anisotropies, we expect a negligible influence of the grid anisotropy on the shape of the crystals.

Finally, it can be noted that Bragard et al. [2] used discretization of Laplacian in the phase-field equation by means of the 18-point formula. This allows for reaching more isotropic approximation of the crystal shape with its lower dependence on the grid anisotropy. Therefore even smaller influence of grid anisotropy can be expected with high-order approximation of differential operators introduced into the system of governing equations.

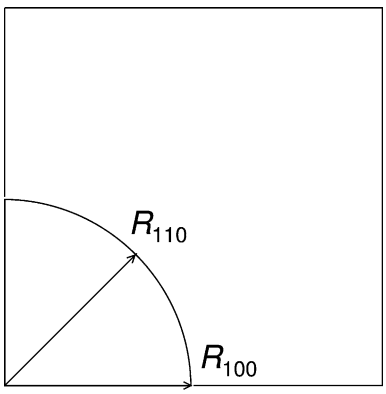

Fig. 3. Simulation setup for the investigation of grid anisotropy displaying the direction of the measured radii R_{100} and R_{110} in the crystallographic directions ⟨1 0 0⟩ and ⟨1 1 0⟩, respectively.

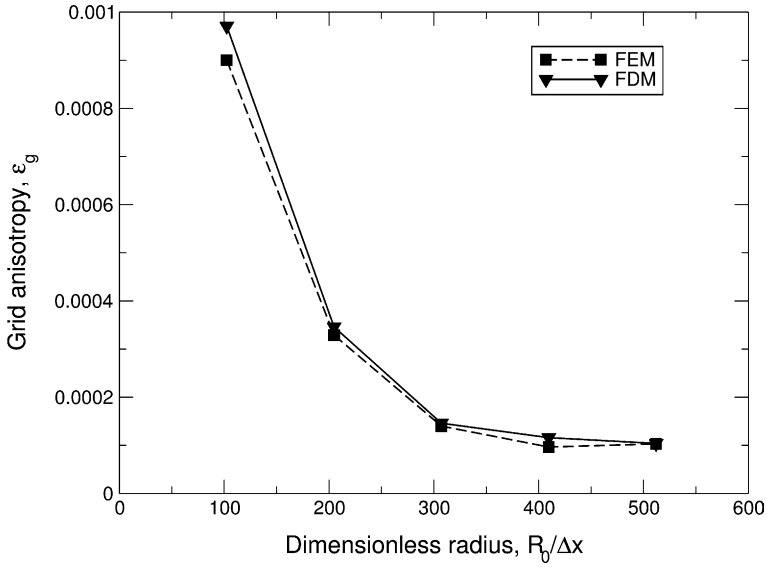

Fig. 4. Plot of the grid anisotropy ε_g measured for FDM and FEM simulations depending on the initial radius R_0 of a spherical isotropic crystal.

6. Simulation of dendritic structures

The formation of dendritic structures in materials depends sensitively on the effect of both, surface energy and kinetic anisotropy of the solid–liquid interface. In this section, we apply our numerical methods for solving the phase-field equations (20) and (21) to model 2D and 3D dendritic crystallization of undercooled nickel melts. In particular, we compare the simulated steady-state growth dynamics (tip velocity) and growth characteristics (tip radii) with the analytical predictions of Brener [3]. We additionally validate the simulated variation of growth velocity for different bulk undercoolings by a comparison with very recent experimental measurements [4,5]. The experiments were conducted with nickel droplets using the electromagnetic levitation technique. Furthermore, we present a spectrum of different morphologies in 3D to demonstrate the fundamental influence of the anisotropy and of the undercooling.

6.1. Comparison with the Brener theory and with experimental results

Efim Brener analytically investigated the effect of surface energy and kinetic anisotropy on the velocity of growing dendrites in pure substances [3]. The author derives scaling laws for the dendrite tip velocity v and for the dendrite tip radius R in correlation with the strength of both anisotropies. We apply the phase-field model to solidification of pure nickel dendrites in order to compare the simulated tip velocity and the tip radius for different undercoolings with the appropriate analytical values for nickel proposed by Brener. For this comparison, we briefly report the relevant analytical expressions for v and for R in the presence of anisotropic strengths:

$$v = \frac{\epsilon_k^{5/4} P_T}{\eta \beta_0} \quad \text{and} \quad R = \eta_R \epsilon_c^{-7/4} \frac{d_0}{P_T}, \tag{26}$$

where $P_T = vR/(2a)$ is the thermal Peclet number. η and η_R can be determined from analytical asymptotics as discussed in [3,34]. Using Ivantsov's relation, the dependences of the dimensionless undercooling Δ on the thermal Peclet number P_T in 2D and 3D read

$$\Delta_{2D}(P_T) = 2\sqrt{P_T}\exp(P_T)\int_{\sqrt{P_T}}^{\infty}\exp(-x^2)\mathrm{d}x, \tag{27}$$

$$\Delta_{3D}(P_T) = P_T\exp(P_T)\int_{P_T}^{\infty}\frac{\exp(-x)}{x}\mathrm{d}x. \tag{28}$$

Consequently, the value of the Peclet number P_T can be obtained for a unique undercooling Δ in Eqs. (27) and (28). Herewith, the velocity v and the radius R of the dendritic tip can be determined by inserting P_T into Eq. (26). For the subsequent comparison between the analytical solution and the data from phase-field simulations we remark the following points: Brener derived various asymptotic solutions for the relations between the strengths of the physical anisotropies and different levels of magnitude of the Peclet number to distinguish sluggish and fast growth kinetics. We chose the scalings for the growth regime consistent with moderate and high dendrite velocities equivalent with high thermal Peclet numbers. Furthermore, the theory in [3] has originally been developed for 2D growth of dendrites. However, the scalings of Eq. (26) can also be applied to 3D growth [35]. The only difference for 2D and 3D growth of dendrites lies in the determination of the parameters η and η_R.

For comparison of the velocity-undercooling relation in Fig. 5, we consider η to be a fitting parameter and adjust its value corresponding to the growth velocity in 2D and 3D using the results of phase-field

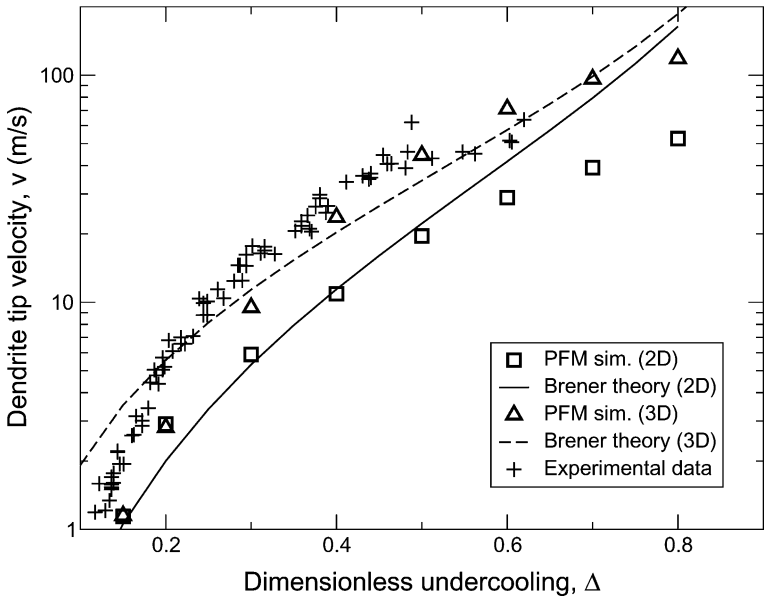

Fig. 5. Tip velocity of nickel dendrites plotted against the dimensionless undercooling Δ for the material parameters "data set 1" given in Tables 1 and 2. The data of 2D and 3D phase-field simulations (squares and triangles) are shown in comparison with the theoretical predictions by Brener [3] (dashed line and solid line) for fitting parameters $\eta \simeq 0.124$ (2D) and $\eta \simeq 0.262$ (3D) computed from Eq. (29). The simulation results are obtained from numerical solving Eqs. (20) and (21). The recently measured experimental data of pure nickel solidification (crosses) [4,5] confirm the simulation results in the undercooling range $0.4 \leqslant \Delta \leqslant 0.6$.

modelling and the following approximation procedure. To determine η, we define an error criterion measuring the deviation between analytical and numerically simulated predictions for the velocities v

$$E_v = \sum_k \left(\frac{v(\Delta_k) - v_k^{\mathrm{sim}}}{v(\Delta_k)} \right)^2, \tag{29}$$

where the sum is taken over the set of undercoolings Δ_k used in the simulations, and v_k^{sim} are simulated values. The fitting parameters are obtained by minimizing the error function $E_v(\eta)$ with respect to η. Solving the equation $\mathrm{d}E_v/\mathrm{d}\eta = 0$ gives the values $\eta \simeq 0.124$ for the 2D and $\eta \simeq 0.262$ for the 3D data sets. Inserting these values into the scaling Eq. (26) leads to the comparison between numerical and analytical results displayed in Fig. 5 for 2D and 3D growth. In addition to this, the diagram contains recent experimental measurements of the velocity of dendritic solidification of pure nickel melts (reported in [4,5]).

Within a range of low and moderate undercoolings $0.3 \leqslant \Delta \leqslant 0.6$ and $0.15 \leqslant \Delta \leqslant 0.5$ the simulated tip velocities v match well with the Brener theory in 2D and 3D, respectively.

The derivation of the Brener's theory is based on the assumption of small Peclet numbers and small anisotropy parameters. For high undercoolings the Peclet number is high and the anisotropy of the kinetic, $\epsilon_{\mathrm{k}} = 0.13$, is important. Hence, the assumptions of the Brener theory cause the discrepancy between the theoretical predictions and the numerical results for undercoolings $\Delta \geqslant 0.6$ in Fig. 5. For 3D dendrites, the experimentally measured data also agree well with the phase-field simulations over the considered undercooling interval $0.4 \leqslant \Delta \leqslant 0.6$. For small undercoolings $0.15 \leqslant \Delta < 0.40$, the disagreement between the experimental data and the phase-field model predictions is attributed to the influence of the forced convective flow in the droplets [5] and to tiny amounts of impurities in the "nominally pure" nickel samples during the experimental procedure of measurements [4,5]. According to the analysis in [36], the convective flow in the droplets enhances the growth velocity in the range of small undercoolings, so that the tip velocity of the dendrites is comparable to the velocity of the liquid flow.

In Fig. 6, we illustrate the sensitivity of the a numerical velocity-undercooling results on (a) the material parameters and on (b) the code used to perform the simulations. In particular, we compare the velocity values obtained for the data set 1 and for the data set 2 in Tables 1 and 2. Further, the deviation of the computed values with respect to the results stated in [2] are shown. It can be seen that the underlying thermophysical data set has a significant and pronounced influence on the computed velocity, especially for low undercoolings ($\Delta < 0.4$) whereas the implemented code shows only minor differences in the results.

The diagram in Fig. 7 shows the simulated tip radii (open squares) in comparison with three analytical Brener curves for different values of the fitting parameter η_{R} in Eq. (26) and for the 2D case. The tip radius decreases at higher undercoolings and equivalently at higher dendrite tip velocities. A deviation of the computed radii with respect to the theoretical curves can be observed irrespectively of the choice of the fitting parameter η_{R}. We assume the discrepancy is due to the fact that the tip radius is a more sensitive parameter for approximating an analytical derivation than a kinetic parameter such as the velocity.

6.2. Dendritic structures

In the numerical simulations in Fig. 8, we obtained a morphological spectrum of different interfacial crystal structures for a range of undercoolings $\Delta = 0.15,\ldots,1.0$. The results show a transition from grained crystals at small undercoolings $\Delta \leqslant 0.15$ to dendritic patterns at intermediate undercoolings $0.15 < \Delta < 1.0$ changing again to grained crystals at high undercoolings $\Delta \geqslant 1.0$. Within the range of intermediate undercoolings, the shape of the dendrites is dictated by the preferred crystallographic direction. For the case of nickel, the dendrites grow in the $\langle 1\,0\,0 \rangle$ direction even though both physical anisotropies act during growth simultaneously.

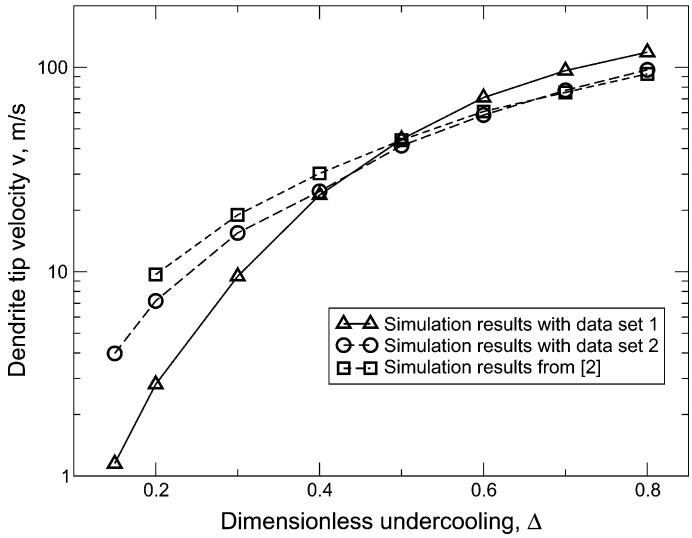

Fig. 6. Simulation results of the dendritic tip velocity as a function of the undercooling for the two different data sets in Tables 1 and 2 and for different programme codes. The triangles correspond to the data set 1 and the code of the authors, the open circles correspond to the data set 2 and the code of the authors, whereas the squares correspond to the data set 2 and the code used for the simulation results discussed in [2].

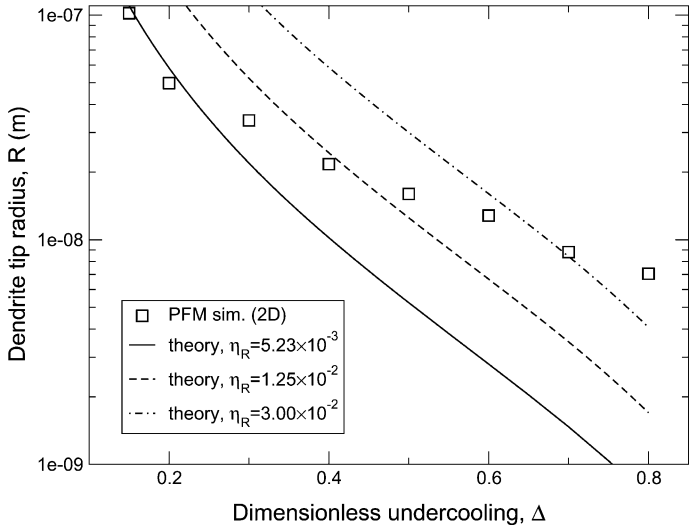

Fig. 7. Tip radius of nickel dendrites as a function of the dimensionless undercooling Δ. The phase-field simulations (open squares) are compared with the analytical theory in Eq. (26) by Brener [3] for three different fitting parameters η_R and for the 2D case.

The role of anisotropy for selecting and stabilizing dendritic structures has been studied analytically in [37,38]. In the presence of both, surface energy and kinetic anisotropy, a stable growth mode of dendrites is found for arbitrary undercoolings [34]. As classified in [34,39], the so-called surface tension needle crystals occur at small and moderate undercoolings. At higher undercoolings, kinetic needle crystals grow due to

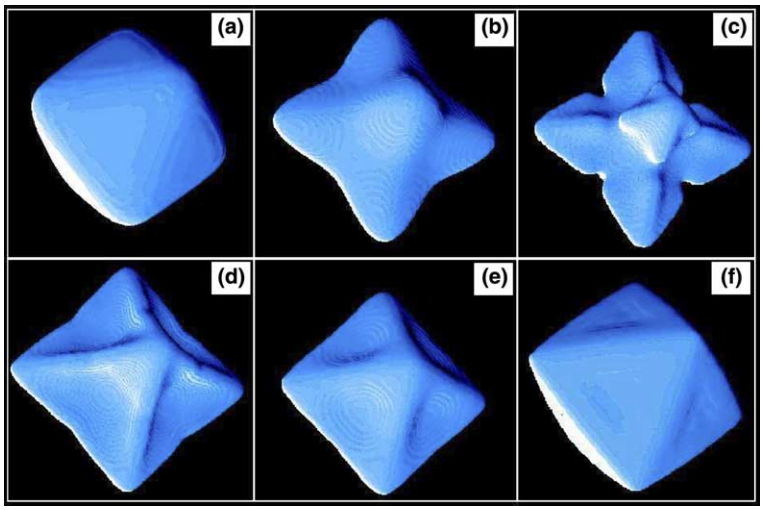

Fig. 8. Simulated morphologies for different initial undercoolings: (a) $\Delta = 0.15$; (b) $\Delta = 0.25$; (c) $\Delta = 0.50$; (d) $\Delta = 0.75$; (e) $\Delta = 0.85$; (f) $\Delta = 1.00$. The material parameters used are given in Tables 1 and 2 on a numerical grid of size 450^3.

the anisotropy of the atomic kinetics. As soon as one of the anisotropies vanishes, one may expect a degeneration of the stable dendritic growth within the considered range of undercoolings.

Fig. 9 demonstrates the morphological spectrum of crystals modelled with a zero kinetic anisotropy $\epsilon_k = 0$ and with a finite anisotropy of the interfacial energy $\epsilon_c \neq 0$. The structure of the branched dendritic crystal for an undercooling of $\Delta = 0.30$ is similar to the shape found with both anisotropies at a relatively

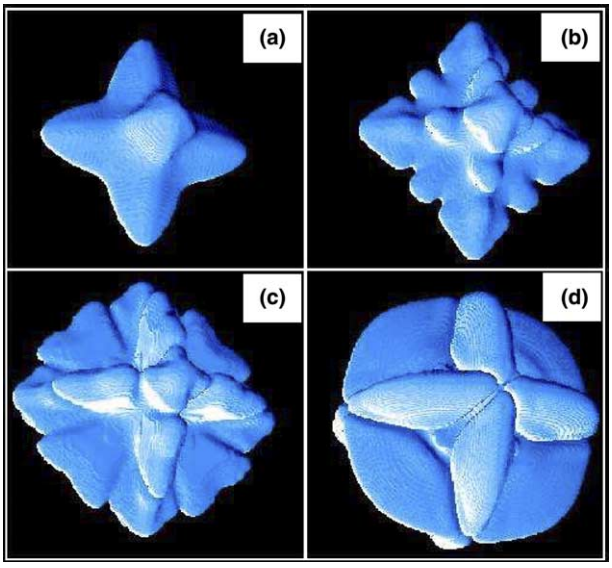

Fig. 9. Morphological spectrum of dendritic structures for different initial undercoolings: (a) $\Delta = 0.30$; (b) $\Delta = 0.45$; (c) $\Delta = 0.55$, and (d) $\Delta = 0.8$. The computations were performed with anisotropies $\epsilon_k = 0$ and $\epsilon_c = 0.018$. The patterns are simulated on a grid of size 450^3.

small undercooling of $\Delta = 0.25$ in Fig. 8(b). At higher undercoolings, the interfacial anisotropy does not compensate the appearance of new branches in directions others than the preferred $\langle 1\,0\,0 \rangle$ crystallographic direction, Fig. 9(b)–(d). In the simulations, we find that the onset of the transition from surface

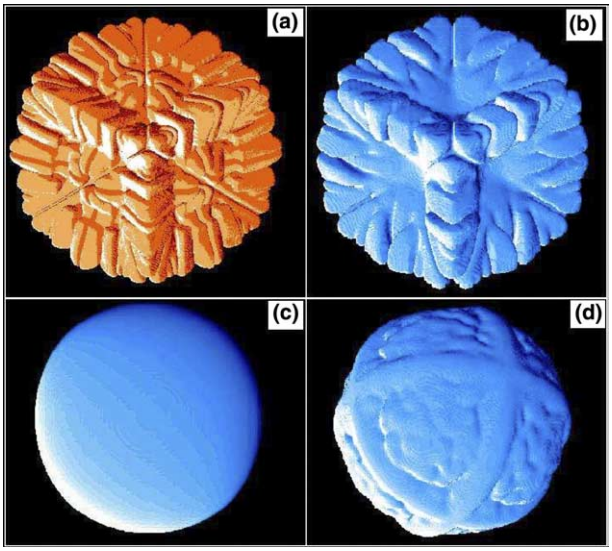

Fig. 10. Patterns observed for zero anisotropies $\epsilon_c = \epsilon_k = 0$ on a numerical grid of size 550^3. The top line shows the formation of fractal crystals at dimensionless undercoolings: (a) $\Delta = 0.70$ and (b) $\Delta = 0.80$. At higher undercoolings, spherical structures occur as shown in the bottom line: (c) $\Delta = 1.20$ with no thermal noise and (d) $\Delta = 1.10$ with induced thermal noise.

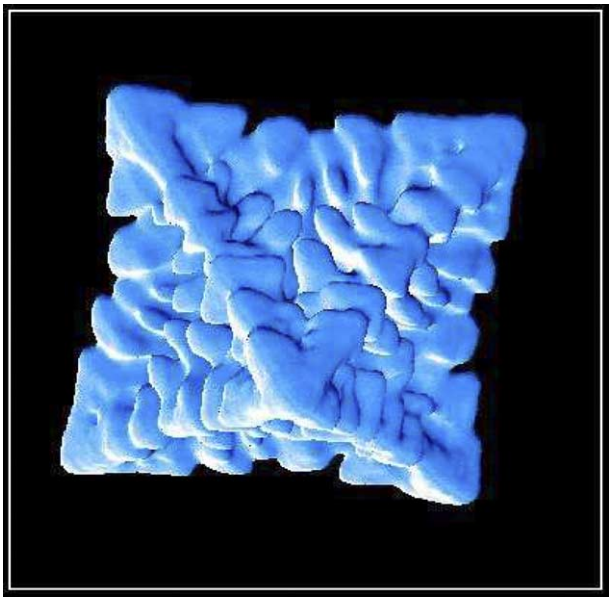

Fig. 11. Computed nickel dendrite using the physical data given in Tables 1 and 2. The undercooling was set to $\Delta = 0.55$ and thermal noise was induced. The computational domain has a size of 650^3 numerical grid points.

tension needle crystals to kinetic needle crystals occurs at a dimensionless undercooling of $\Delta = 0.42$ for pure nickel.

Branched crystals of fractal type develop for zero anisotropies of the surface energy $\epsilon_c = 0$ and of the kinetic coefficient $\epsilon_k = 0$ as shown in Fig. 10(a)–(b). A so-called "triplet" consisting of three cooperating symmetry-broken fingertips forms at the center of the fractal-like structure. Triplets may be observed in 3D instead of doublons predicted for 2D. Such triplets were first modelled as dynamically stable objects in a 3D space using the phase-field method in [40]. We observe that the triplets disappear with a further increasing of the undercooling. Beyond the hypercooling limit of $\Delta > 1.0$, smooth spherical structures grow as crystals without any anisotropy (see Fig. 10(c)–(d)).

It is known that stochastic noise may influence the amplitude of the side branches [41,42]. Moreover, the noise plays a crucial role for the formation of branched crystal patterns of dendritic type [43,44]. Inclusion of the stochastic thermodynamic noise into the phase-field formulation allows modelling of well branched dendritic morphologies [45]. Fig. 11 displays a simulated 3D dendritic crystal with the formation of secondary branches in the presence of thermal noise as proposed via the thin interface analysis in [46]. The noise-induced side branching leads to realistic dendritic structures well-known from natural observations and from experimental studies of metallic systems.

7. Conclusions

As a starting point of our consideration, we used the phase-field model for multicomponent systems [1] which has been reduced in Section 2 to the model for a one-component system with the thin interface asymptotic of Bragard et al. [2]. The phase-field method was applied to simulate crystal growth structures of a pure material in 2D and 3D at low, moderate, and high undercoolings. Finite difference method (FDM) and adaptive finite element method (FEM) were used for solving the evolution equations of the system. Overall, the simulation results demonstrate the unique ability of the phase-field method to simulate solidification microstructures that are well comparable with theoretical predictions and experimental measurements. As particular cases, the following conclusions can be drawn upon the evaluation of the simulation results.

In numerical computations, we compared the approximation behaviour of two asymptotics: The standard phase-field and the thin interface phase-field model by investigating the dynamics of a planar solid–liquid front at different undercoolings. The thin interface approximation has better convergence properties, in particular if the diffuse interface thickness is greater than the microscopic capillary length ($W_0 > d_0$).

The effect of grid anisotropy is analyzed for both numerical methods: FDM and FEM. The numerical grid has no significant influence on the structure formation if the dimensionless radius of a crystal is greater than 100 grid spacings or the growth proceeds under the influence of surface energy and of interfacial kinetic anisotropy.

By 2D and 3D simulations, the influence of the anisotropy and of the undercooling on the morphology, on the dynamics and on the characteristic microstructure quantities is examined. Taking the material data for nickel (see Tables 1 and 2), we find a good agreement between the simulated dendrite velocities and the appropriate 2D and 3D Brener theory [3] for dimensionless undercoolings $\Delta = 0.3,\ldots,0.6$. Furthermore, our simulation results of the tip velocity in 3D are consistent with recent experimental measurements [4,5] within the same range of undercoolings. For the correlation between the tip radius and the undercooling, we observe a strong difference between the Brener theory predictions and the simulation results (Fig. 7) for the dimensionless undercoolings $\Delta > 0.3$. Varying the undercooling and the contributions of the kinetic and of the surface energy anisotropy, we presented a variety of 3D morphologies involving grained, fractal, dendritic and spherical crystals (see Figs. 8–11).

Acknowledgements

The authors thank Mathis Plapp for valuable and intensive discussions to improv the manuscript. Useful exchanges with Efim Brener, Dieter Herlach and Heiner Müller-Krumbhaar are acknowledged with great thanks. This work was performed with support from the German Research Foundation (DFG – Deutsche Forschungsgemeinschaft) under the projects Nos. He 1601/13 and Ne 822/2.

References

[1] H. Garcke, B. Nestler, B. Stinner, A diffuse interface model for alloys with multiple components and phases, SIAM J. Appl. Math. 64 (3) (2004) 775–799.
[2] J. Bragard, A. Karma, Y.H. Lee, M. Plapp, Linking phase-field and atomistic simulations to model dendritic solidification in highly undercooled melts, Interface Sci. 10 (2-3) (2002) 121–136.
[3] E.A. Brener, Effects of surface energy and kinetics on the growth of needle-like dendrites, J. Crystal Growth 99 (1990) 165–170.
[4] D.M. Herlach, O. Funke, G. Phanikumar, P. Galenko, Free dendrite growth in undercooled melts: experiements and modelling. In: M. Rappaz, C. Beckermann, R. Trivedi (Eds.), Solidification Processes and Microstructures: A Syposium in Honor of Prof. Wilfried Kurz. Proceedings of the TMS Annual Meeting, March 14–18, 2004, Charlotte, North Carolina. TMS, Warrendale, Pennsylvania, 2004, pp. 277–288.
[5] O. Funke, G. Phanikumar, P.K. Galenko, M. Kolbe, D.M. Herlach, Dendrite growth velocities during solidification of levitated undercooled nickel melts, European Physical Journal B, submitted for publication.
[6] R.S. Feigelson (Ed.), Progress in Crystal Growth. Proceedings of the Symposium, Seattle, WA, USA, 4–9 August 2002. J. Cryst. Growth 264 (2004) 499–649.
[7] A.A. Chernov, Notes on interface growth kinetics 50 years after, Burton cabrera and frank, J. Cryst. Growth 264 (2004) 499–518.
[8] G.J. Fix, Phase-field methods for the free boundary problems. In: A. Fusano, M. Primicerio (Eds.), Free Boundary Problems: Theory and Application, second ed., Pitman, Boston, 1983, pp. 580–589.
[9] J.B. Collins, H. Levine, Diffuse interface model of diffusion-limited crystal growth, Phys. Rev. B 31 (1985) 6119–6122.
[10] G. Caginalp, An analysis of a phase-field model of a free boundary, Arch. Rat. Mech. Anal. 92 (1986) 205–245.
[11] J.S. Langer, Models of pattern formation in first-order phase transitions, in: G. Grinstein, G. Mazenko (Eds.), Directions in Condensed Matter Physics, World Scientific, Philadelphia, 1986, pp. 165–216.
[12] O. Penrose, P.C. Fife, Thermodynamically consistent models of phase-field type for the kinetics of phase transitions, Physica D 43 (1990) 44–62.
[13] W.J. Boettinger, J.A. Warren, C. Beckermann, A. Karma, Phase-field simulations of solidification, Annu. Rev. Mater. Res. 32 (2002) 163–194.
[14] G. Caginalp, E.A. Socolovsky, Phase-field computation of single needle crystals, crystal growth, and motion by mean curvature, SIAM J. Sci. Comput. 15 (1994) 106–126.
[15] R. Kobayashi, Modelling and numeric simulations of dendritic crystal growth, Physica D 63 (1993) 410–423.
[16] A. Karma, Phase-field methods, in: K.H.J. Buschow, R.W. Cahn, M.C. Flemings, B. Ilschner, E.J. Kramer, S. Mahajan (Eds.), Encylclopedia of Materials: Science and Technology, vol. 7, Elsevier, Oxford, 2001, pp. 6873–6886.
[17] A. Karma, W.-J. Rappel, Quantitative phase-field modelling of dendritic growth in two and three dimensions, Phys. Rev. E 57 (1998) 4323–4349.
[18] M. Plapp, A. Karma, Multiscale finite-difference-diffusion Monte–Carlo method for simulating dendritic solidification, J. Comput. Phys. 165 (2000) 592–619.
[19] M. Barth, F. Joo, B. Wei, D.M. Herlach, Measurement of the enthalpy and specific heat of undercooled nickel and iron melts, J. Non-Crystalline Solids 156-158 (1993) 398–401.
[20] K. Eckler, Dendritisches Wachstum in unterkühlten Metallschmelzen, Ph.D. Thesis, Ruhr-Universität Bochum, 1992.
[21] M. Schwarz, Kornfeinung durch Fragmentierung von Dendriten, Ph.D. Thesis, Ruhr-Universität Bochum, 1998.
[22] J.J. Hoyt, B. Sadigh, M. Asta, S.M. Foiles, Kinetic phase field parameters for Cu–Ni system derived from atomistic computations, Acta Mater. 47 (1999) 3181–3187.
[23] J.J. Hoyt, M. Asta, A. Karma, Method for computing the anisotropy of the solid–liquid interfacial free energy, Phys. Rev. Lett. 86 (2001) 5530–5533.
[24] J.J. Hoyt, M. Asta, A. Karma, Atomistic and continuum modelling of dendritic solidification, Mater. Sci. Eng. R 41 (6) (2003) 121–153.
[25] S.R. Coriell, D. Turnbull, Relative roles of heat transport and interface rearrangement rates in the rapid growth of crystals in undercooled melts, Acta Metall. 30 (1982) 2135–2139.

[26] J.Q. Broughton, G.H. Gilmer, K.A. Jackson, Crystallization rates of a Lennard-Jones liquid, Phys. Rev. Lett. 49 (1982) 1496–1500.
[27] P.K. Galenko, D.A. Danilov, Local nonequilibrium effect on rapid dendritic growth in a binary alloy melt, Phys. Lett. A 235 (1997) 271–281.
[28] P.K. Galenko, D.A. Danilov, Model for free dendritic alloy growth under interfacial and bulk phase nonequilibrium conditions, J. Cryst. Growth 197 (1999) 992–1002.
[29] R. Hultgren, P.D. Desai, D.T. Hawkins, M. Gleiser, K.K. Kelley, D. Wagman, Selected Values of the Thermodynamic Properties of the Elements, ASM, Metals Park, OH, 1973.
[30] M. Plapp, private communication.
[31] H. Garcke, B. Nestler, B. Stoth, Interfaces Free Boundaries 1 (1999) 175–198.
[32] N. Provatas, N. Goldenfeld, J. Dantzig, Adaptive mesh refinement computation of solidification microstructures using dynamic data structures, J. Comput. Phys. 148 (1999) 265–290.
[33] W. Bangerth, G. Kanschat, Concepts for object-oriented finite element software – the deal II library, Preprint 99-43 (SFB 359), IWR Heidelberg (October 1999).
[34] E. Brener, V.I. Melnikov, Pattern selection in two-dimensional dendritic growth, Adv. Phys. 40 (1991) 53–97.
[35] M. Ben Amar, E. Brener, Theory of pattern selection in three-dimensional nonaxisymmetric dendritic growth, Phys. Rev. Lett. 71 (1993) 589–592.
[36] P. Galenko, D. Herlach, G. Phanikumar, O. Funke, Phase-field modelling of dendritic solidification in undercooled droplets, in: P. Vincenzini, A. Lami (Eds.), Computational Modelling and Simulation of Materials. Proceedings of 3rd International Conference, Acireale, Italy, 30 May–4 June, 2004, Techna Group Publishers, Faenza, Italy, 2004, pp. 565–572.
[37] J.S. Langer, D.C. Hong, Solvability conditions for dendritic growth in the boundary-layer model with capillary anisotropy, Phys. Rev. A 34 (1986) 1462–1471.
[38] M. Ben Amar, P. Pelce, Impurity effect on dendritic growth, Phys. Rev. A 39 (1989) 4263–4269.
[39] F. Liu, N. Goldenfeld, Instability of needle crystals in anisotropic dendritic growth, Phys. Rev. A 42 (1990) 5052–5055.
[40] T. Abel, E. Brener, H. Müller-Krumbhaar, Three-dimensional growth morphologies in diffusion-controlled channel growth, Phys. Rev. E 55 (1996) 7789–7792.
[41] A. Dougherty, P.D. Kaplan, J.P. Gollub, Development of side branching in dendritic crystal growth, Phys. Rev. Lett. 58 (1987) 1652–1655.
[42] J.S. Langer, Dendritic sidebranching in the three-dimensional symmetric model in the presence of noise, Phys. Rev. A 36 (1987) 3350–3358.
[43] E. Brener, D. Temkin, Noise-induced sidebranching in the three-dimensional nonaxisymmetric dendritic growth, Phys. Rev. E 51 (1995) 351–359.
[44] U. Bisang, J.H. Bilgram, Shape of the tip and the formation of sidebranches of xenon dendrites, Phys. Rev. Lett. 75 (1995) 3898–3901.
[45] S.G. Pavlik, R.F. Sekerka, Forces due to fluctuations in the anisotropic phase-field model of solidification, Physica A 286 (1999) 283–290.
[46] A. Karma, W.-J. Rappel, Phase-field model of dendritic sidebranching with thermal noise, Phys. Rev. E 60 (1999) 3614–3625.